Journal of Alloys and Compounds 1036 (2025) 181217

Contents lists available at ScienceDirect

Journal of Alloys and Compounds

journal homepage: www.elsevier.com/locate/jalcom

Research article

New insights into the role of the doping process on the luminescence properties of MgB_4O_7:Ce,Li

Jorge L.O. Santos [a], Adelmo S. Souza [a], João V.B. Valença [b], Henrique Trombini [b], Cláudio Radtke [c], Iury S. Silveira [d], Roger G. Fernandes [e], Heveson Lima [f],*

[a] Centro Multidisciplinar de Bom Jesus da Lapa, Universidade Federal do Oeste da Bahia, Bom Jesus da Lapa, 47600-000, BA, Brazil
[b] Grupo de Física Médica Experimental e Computacional, Universidade Federal de Ciências da Saúde de Porto Alegre, Porto Alegre, 90050-170, RS, Brazil
[c] Instituto de Química, Universidade Federal do Rio Grande do Sul, Porto Alegre, 91509-900, RS, Brazil
[d] Instituto de Pesquisas Energéticas e Nucleares, São Paulo, 05508-000, SP, Brazil
[e] Laboratório Nacional de Luz Síncrotron, Centro Nacional de Pesquisa em Energia e Materiais, Campinas, 13083-100, SP, Brazil
[f] Centro Multidisciplinar de Luís Eduardo Magalhães, Universidade Federal do Oeste da Bahia, 47855-218, Luís Eduardo Magalhães, BA, Brazil

ARTICLE INFO

Keywords:
MgB_4O_7
Thermoluminescence
Synchrotron radiation
Luminescence
Radiation dosimetry

ABSTRACT

Magnesium tetraborate (MgB_4O_7) has garnered significant attention in recent years for ionizing radiation dosimetry applications. Despite advances in the material's performance, the fundamental mechanisms underlying lithium (Li) and cerium (Ce) doping and co-doping remain unclear in the literature. In this study, we comprehensively investigate the role of Li and Ce doping in modulating the luminescence behavior of MgB_4O_7. To elucidate the underlying mechanisms, we employed an advance multi-technique characterization approach using nuclear reaction analysis, synchrotron-based X-ray nanospectroscopy, X-ray photoelectron spectroscopy (XPS), thermoluminescence (TL) spectrum emission, and photoluminescence (PL) spectroscopy. We have shown that Li remains into the host matrix during the synthesis, being associated with shallow traps such as F^{2+} center. Also, approximately 50% of Ce^{4+} is reduced to Ce^{3+} on the material's surface, forming complex defect structures involving Ce ions and F-center. Additionally, we present strong evidence that the TL emission around 580 nm originates from F-centers rather than trace Mn elements. Some mechanisms that compete simultaneously with each other have been proposed. Our integrated strategy provides insights into the complex dopant-induced electronic and optical transformations in MgB_4O_7, offering a detailed understanding of the material's luminescence characteristics.

1. Introduction

Luminescent materials play an important role in various technological applications, ranging from optoelectronics to ionizing radiation dosimetry [1–3]. Among these, magnesium tetraborate (MgB_4O_7) is a crystalline matrix, with an orthorhombic structure and Pbca space group [4], which has long attracted interest due to its promising characteristics for application in dosimetry, particularly in personal dosimetry. Notable features include an effective atomic number ($Z_{eff} = 8.4$) comparable to human tissue – reducing the need for correction factors in dose analysis –, a linear dose response up to ~10 Gy and saturation occurring above ~1000 Gy [5], and the presence of Boron, which enables the use of B-10 in sample production, taking advantage of its high cross-section with thermal neutrons.

When doped with specific rare-earth and alkali elements, MgB_4O_7 exhibits significantly enhanced stimulated luminescent emission [6–8]. Regarding specifically to the optically stimulated luminescence (OSL) emission, it can achieve levels comparable to the commercial available dosimeter based on Al_2O_3:C [9]. This enhanced performance makes it an ideal candidate for advanced applications when connected to techniques such as OSL. Understanding the origin and fundamental mechanisms governing the luminescence of the doped/co-doped MgB_4O_7 is essential for optimizing its performance in radiation dosimetry, a field that demands material characteristics such as high sensitivity, stability, and reproducibility. The luminescent response of MgB_4O_7, particularly when doped and co-doped respectively with Ce and Li, is influenced by intricate defect structures, charge trapping dynamics, and eventually energy transfer processes. To the best of the authors' knowledge, a complete understanding of the origin and mechanism of emission in this material is still lacking.

Recent studies have focused on the synergistic effects of Li and Ce dopants on MgB_4O_7's luminescent properties, particularly how Li co-doping enhances OSL signal intensity and influences defect clustering

---

* Corresponding author.
E-mail addresses: jlosantos@ufob.edu.br (J.L.O. Santos), heveson.matos@ufob.edu.br (H. Lima).

https://doi.org/10.1016/j.jallcom.2025.181217
Received 29 March 2025; Received in revised form 16 May 2025; Accepted 24 May 2025

structure with Ce ions [5,10–14]. Some analyses suggest that Li may acts as a charge compensator, facilitating the substitution of Mg^{2+} by Ce^{3+} [5,10]. This assumption is based on the idea that Ce^{3+} is the predominant state in the host matrix. However, it is important to note that cerium ions can exist in either the 3+ ([Xe]$4f^1$) and 4+ ([Xe]$4f^0$) valence state. The stability of these oxidation states varies significantly depending on the chemical environment, as demonstrated in electrochemical redox studies [15–17]. Recent research has shown that the choice of cerium precursor significantly influences Ce^{3+} content in synthesized materials and, consequently, the amount of oxygen vacancies on the material's surface [15,18–20]. For instance, $Ce(NO_3)_3$ yields a higher proportion of Ce^{3+} compared with other precursors such as $Ce(OH)_4$ and $Ce(COOCH_3)_3{\cdot}5H_2O$ [19]. Plokhikh et al. analyzed the influence of doping and co-doping on the MgB_4O_7:Ce (0.3 mol%), Li (10 mol%) produced via solid-state synthesis, using different cerium sources: cerium (IV) oxide and cerium (III) nitrate. They estimated 32% Ce^{3+} in the sample synthesized from CeO_2 and 74% Ce^{3+} in the sample synthesized from $Ce(NO_3)_3$ [14], highlighting the significant influence of the chemical environment on Ce^{3+} content.

Optimal dopant concentrations have been established through various studies in the literature. Using Solution Combustion Synthesis, researchers identified optimal concentrations of 10 mol% for Li and 0.3 mol% for Ce [5], corresponding to approximately 0.39 wt% and 0.24 wt%, respectively. The enhanced OSL intensity at these concentrations, up to 10 mol%, without significant changes in the MgB_4O_7 phase, was initially attributed to Li loss during synthesis. However, this hypothesis is not supported by available data, as the limited sensitivity of X-ray diffraction (XRD) analysis in identifying phases at concentrations below 5 wt% casts doubt on this explanation. Optimal concentrations of 0.5 wt% for both Li and Ce were reported by Souza et al. [11] using solid-state synthesis, with OSL signal quenching observed at higher Li concentration.

A persistent mystery in the literature concerns a broad thermoluminescence (TL) emission band at 550 nm in MgB_4O_7:Ce,Li. Yukihara et al. attributed this broad TL emission to Mn impurities, resulted from Mn contamination of the magnesium nitrate precursor [6]. In the same study, a high-purity magnesium nitrate (99.999% purity) was used to synthesize the compound. The absence of the broad TL emission led the authors to conclude that this peak was indeed associated with Mn impurities. However, Souza et al. [11] also observed a broad TL emission around 550 nm when starting with a MgO precursor (Merck, 99.9% purity) instead of magnesium nitrate. Additionally, Batista et al. [12] employed Particle-induced X-ray emission (PIXE) and detected Mn concentration at trace levels in Ce-co-doped MgB_4O_7 (MgO from Alphatec with 99% purity), with concentrations significantly lower than those other impurities such as Ca, Si, and Al. For MgB_4O_7:$Ce_{0.33wt\%}Li_{0.67wt\%}$, for instance, the elemental concentration was measured at 24 ± 10 ppm, near the limit of detection. These findings cast doubt about Mn's role as a trace element responsible for the broad TL emission in 550 nm.

These uncertainties highlight the challenges in fully understanding the luminescent mechanisms of Li- and Ce-co-doped MgB_4O_7, in a synergistic manner. Unraveling these mechanisms is crucial for tailoring its thermoluminescent and optically stimulated luminescent properties, enabling more precise and efficient radiation dose measurements in different applications.

In this context, we explore the impact of lithium (Li) and cerium (Ce) on the luminescence behavior of MgB_4O_7:Ce,Li. Using state-of-the-art nuclear reaction analysis, synchrotron-based X-ray nanospectroscopy, X-ray photoelectron spectroscopy (XPS), thermoluminescence (TL) spectrum emission, and photoluminescence (PL) spectroscopy, the aim is to provide novel insights and hypotheses into the structural and electronic modifications induced by varying dopant concentrations and using different reagent as precursors, contributing to the current discussion and paving the way for the development of next-generation luminescent materials.

2. Experimental

2.1. Synthesis of materials

Synthesis of MgB_4O_7 doped and co-doped with Ce and Li at different concentrations was carried out using the solid-state synthesis method. The annealing process was conducted in atmospheric air, using a heating rate of 10 °C/min up to a maximum temperature of 900 °C, with a dwell time of 6 h. The furnace was then turned off and the materials were subjected to a free and slowly cooling process until room temperature was reached (25 °C). During the material production, the following analytical grade reagents were used: MgO (Alphatec, 99% purity), H_3BO_3 (Alphatec, 99.5% purity), CeO_2 (Alpha Aesar, 99.5% purity), and LiCl (Vetec, 99% purity). The produced materials present the following nominal concentrations for the dopants and co-dopants: MgB_4O_7:$Ce_{1.0wt\%}$, MgB_4O_7:$Li_{1.0wt\%}$, MgB_4O_7:$Ce_{0.67wt\%}Li_{0.33wt\%}$, and MgB_4O_7:$Ce_{0.33wt\%}Li_{0.67wt\%}$. The synthesis procedure, as well as the characterization results of the materials used in this study, are presented in a previous work [12].

2.2. Nuclear reaction analysis

The relative amount of lithium in the samples was determined using the $^7Li(p, \alpha)^4He$ nuclear reaction. For this, a 1 MeV proton beam ($^1H^+$) with incidence perpendicularly to the sample surface was used. The beam current was approximately 10 nA, focused on a 2.0 mm diameter spot. The charged particle spectra were recorded using a silicon detector (Canberra, active area: 50 mm^2; nominal depletion depth: 100 μm) positioned at 150° relative to the beam direction. To prevent overlap between the backscattered protons and α particles from the nuclear reaction, a 12 μm Mylar stopper foil was placed between the detector and the sample. Based on the elemental composition of the sample, additional nuclear reactions may contribute to the spectrum, such as $^{10}B(p, \alpha)^7Be$, $^{11}B(p, \alpha)^8Be$, and $^{18}O(p, \alpha)^{15}N$. However, due to the relatively low energies of the α particles produced in these reactions, the corresponding peaks are expected to appear at significantly lower channel numbers in the spectrum. This ensures that the α signal from the $^7Li(p, \alpha)^4He$ reaction does not overlap with those from other nuclear reactions. During the measurements, a device traverses the beam to record the current, ensuring accurate quantification of the total charge incident on the sample. The Li signal was integrated over the same region for each sample, and the resulting area was correlated with the Li content using a lithium tetraborate ($Li_2B_4O_7$) standard from FMaia (São Paulo, Brazil), which has a purity greater than 99%.

2.3. Synchrotron-based X-ray nanospectroscopy

The synchrotron-based nanospectroscopy experiments were conducted at the Coherent X-ray Nanoprobe Beamline (CARNAÚBA) of the Brazilian Synchrotron Light Laboratory (LNLS) [21]. Powder samples were mounted on double-sided carbon tape and afixed to a CARPIN [21]. Measurements were performed in step-scan mode, scanning each sample over a 50 × 50 μm area with a 1 μm pixel size. This approach enables the acquisition of a full spectrum at each pixel, including X-ray fluorescence (XRF) and X-ray excited optical luminescence (XEOL) spectra. Additionally, it allows for hyperspectral imaging, providing spatially resolved emission energy and wavelength distributions. For both XRF and XEOL measurements, the CARNAÚBA beamline's 4CM monochromator was set to an excitation energy of 9725 eV. X-ray fluorescence signals were detected using two silicon drift detectors (Vortex, Hitachi) positioned at 75° and 70° relative to the incident beam. The XEOL signal was collected via an aluminum-coated reflective lens coupled to a collimator (both from ThorLabs), directing the signal into a UV–Vis optical fiber connected to a QE-Pro-ABS spectrometer (Ocean Optics), covering the 200–950 nm range. All XRF and XEOL data, including image generation and spectral fitting, were processed using the PyMCA software package [22].

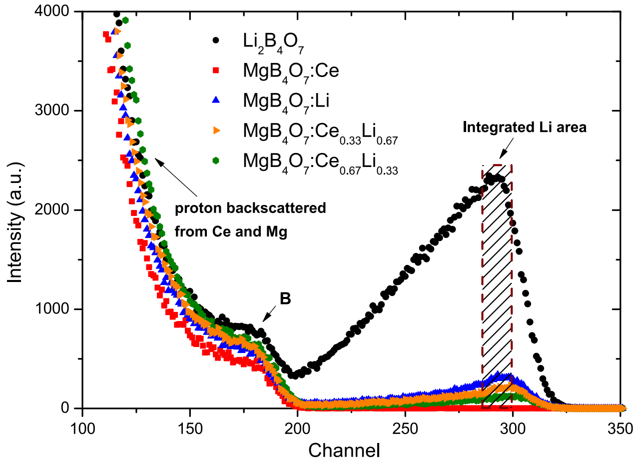

Fig. 1. Nuclear reaction spectra of the samples $Li_2B_4O_7$ (black dots), MgB_4O_7:Ce (red square), MgB_4O_7:Li (blue up-pointing triangle), MgB_4O_7:$Ce_{0.33}Li_{0.67}$ (orange side-pointing triangle), and MgB_4O_7:$Ce_{0.67}Li_{0.33}$ (green octagon) obtained with 1 MeV incoming H^+ ions. The shaved area represents the selected region used to quantify the relative amount of lithium in the samples. Li, B, and H^+ backscattered from Ce and Mg are also indicated. (For interpretation of the references to color in this figure legend, the reader is referred to the web version of this article.)

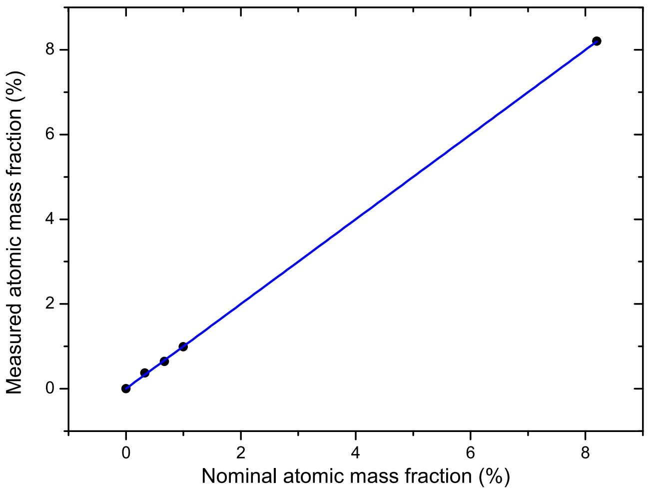

Fig. 2. Nominal vs. measured atomic mass fractions (%) of lithium. Black dots represent the data points, while the blue line denotes the linear fit.

2.4. X-ray photoelectron spectroscopy

XPS spectra were acquired using a Thermo Fisher K-Alpha spectrometer equipped with a monochromatic and micro-focused Al K*α* excitation source (1486.6 eV) with variable spotsize, provided by LNNano/CNPEM, Campinas-SP, Brazil. To minimize background interference and avoid sample contamination, ensuring high-fidelity analysis of the surface chemical composition, the sample was kept in the analysis chamber under an ultra-high vacuum with a base pressure of approximately 5×10^{-10} mbar. Spectra were recorded over a binding energy range of 870 to 930 eV, encompassing the Ce 3d signals.

2.5. Photoluminescence spectroscopy

Photoluminescence emission and excitation spectra were recorded at room temperature using a FluoroMax-Plus-C-P spectrofluorometer from Horiba Scientific. The fluorescence spectra were acquired with an integration time of 0.1 s, and the slit widths for both excitation and emission were set to 1.0 nm.

Table 1
Lithium peak area (a.u.) and the nominal and measured lithium fractions (%) for each studied sample.

Sample	Li peak area (a.u.)	Nominal Li mass fraction (%)	Measured Li mass fraction (%)
$Li_2B_4O_7$	63 983	8.20	8.20
MgB_4O_7:Ce	5	0	0
MgB_4O_7:Li	13 044	1.00	0.99
MgB_4O_7:$Ce_{0.33}Li_{0.67}$	7904	0.67	0.64
MgB_4O_7:$Ce_{0.67}Li_{0.33}$	4850	0.33	0.37

2.6. Thermoluminescence emission spectra

For the acquisition of the TL emission spectra, the photomultiplier tube was removed from the Risøreader system. An optical fiber with a core diameter of 600 μm was then connected to an Ocean Optics QE65 Pro spectrometer with a sensitivity range between 200–1000 nm, which was used to obtain the emitted light signal. The emission spectra were recorded during the heating of the sample from room temperature up to 400 °C, using a heating rate of 5 °C/s, and an integration time of 0.5 s. The samples were previously irradiated with a dose of 10 kGy, using a Gamma-Chamber irradiator, which had a dose rate of 8.55 kGy/h. The data were collected using the Spectra Suite software, by Ocean Optics, and the obtained results are discussed based on a relative comparison of the sample's emission and the wavelengths associated with their emission bands.

3. Results

3.1. Lithium quantification

Fig. 1 shows the nuclear reaction spectra of the samples $Li_2B_4O_7$, MgB_4O_7:$Ce_{1.0wt\%}$, MgB_4O_7:$Li_{1.0wt\%}$, MgB_4O_7:$Ce_{0.33wt\%}Li_{0.67wt\%}$, and MgB_4O_7:$Ce_{0.67wt\%}Li_{0.33wt\%}$ obtained with 1 MeV incoming H^+ ions. The shaved area in Fig. 1 indicates the selected region used to quantify the relative amount of lithium in the samples, ranging from channel 285 to 300. The boron signal starts below channel 200, which means that the Li and B signals will only overlap below that channel, as can be clearly seen in the $Li_2B_4O_7$ sample. The rapid increase in the yield at lower channels comes from the H^+ backscattered from Ce and Mg.

Table 1 shows the integrated Li area, from channel 285 to 300, in arbitrary units (a.u.), along with the nominal and corresponding measured Li fractions (%) for each studied sample. According to Table 1, the maximum difference between the nominal and measured amounts of Li was 11%, observed in the sample with the lowest Li content (MgB_4O_7:$Ce_{0.67wt\%}Li_{0.33wt\%}$). For the MgB_4O_7:$Ce_{1wt\%}$ sample, 5 counts were integrated within the shaved region. These counts were considered electronic noise and subtracted from the other samples. As shown in Fig. 2, the nominal and measured atomic mass fractions of Li exhibit a linear relationship. Even in the sample with the lowest Li content, the NRA results clearly indicate that no Li was lost during synthesis. That means, the strong linear correlation suggests accurate lithium incorporation during synthesis, with no significant losses.

3.2. Synchrotron-based X-ray nanoscopy: STXM, XRF, and XEOL

In this section, we present correlative imaging analysis of Li and Ce co-doped MgB_4O_7, including scanning transmission X-ray microscopy (STXM), X-ray fluorescence (XRF) mapping of Mn and Ce distribution, and X-ray excited optical luminescence (XEOL) emission measured both in total yield and at 764 nm. While STXM results are presented for Li-doped MgB_4O_7, additional analyses are provided in the Appendix for other ones (Figs. A.10 - A.12).

For Li-doped MgB_4O_7, the STXM data (Fig. 3A) revealed higher absorption (lighter areas) around the particle's center, while the XRF mapping (Fig. 3B) showed a non-uniform spatial distribution of Mn

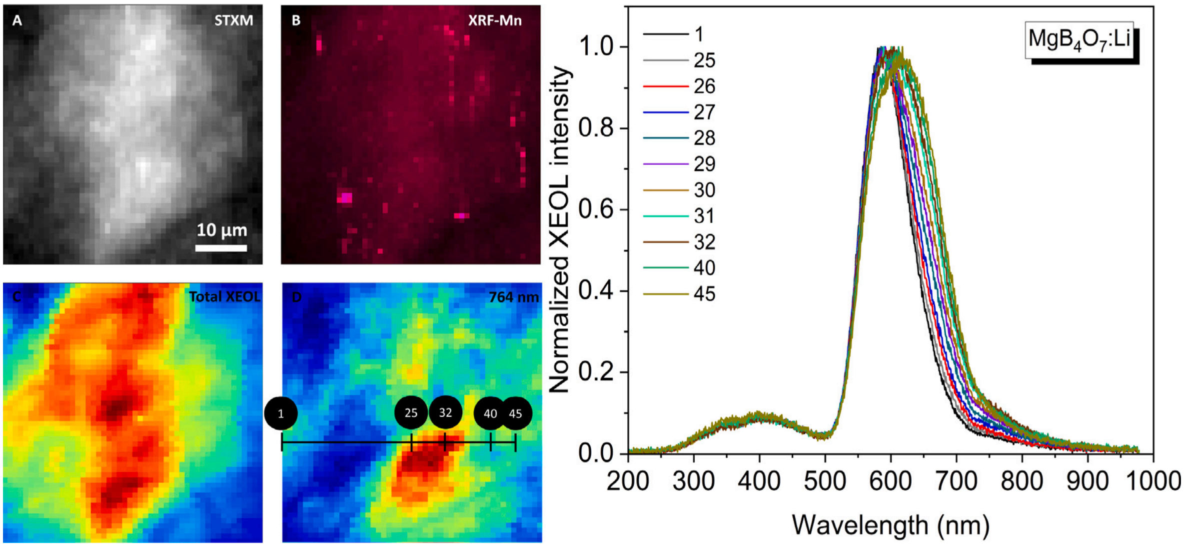

Fig. 3. Correlative STXM, XRF, and XEOL acquisition in MgB_4O_7:Li: (a) STXM; (b) XRF mapping obtained using the Mn K_α emission line. 2D XEOL mapping (c) Total; (d) At 764 nm. XEOL spectrum excited at 9725 eV showed in the right-side. (For interpretation of the references to color in this figure legend, the reader is referred to the web version of this article.)

emission centers, with regions of highest intensity depicted in magenta. Additional trace elements including Ca, Cl, Fe, Ti, Ni, and Co were also detected but are not shown here. Due to technical limitations of the Carnaúba beamline, XRF mapping of low atomic number elements (Mg, B, and Li) could not be performed.

The 2D hyperspectral mapping using total XEOL as contrast revealed an irregular distribution of emission centers, with intense emission regions (shown in red in Fig. 3C/D). The color scale ranges from blue (minimum intensity) to red (maximum intensity). Analysis of the XEOL emission at 764 nm along a horizontal line scan revealed slightly distinct spectral profiles across different regions: consistent patterns between points 1–24; peak broadening between points 25–31, stable emission between points 32–39, and further peak broadening at point 40 extending to longer wavelengths at point 45. These spectral variations, particularly the peak broadening at longer wavelengths, suggest different populations of defect centers in the host matrix. The XEOL spectrum exhibited two broad peaks at 392 nm and 590 nm, and a shoulder at 764 nm.

To investigate synergistic effects of Li and Ce dopants on MgB_4O_7's luminescent properties, we analyzed samples with different proportions of each one (Ce in greater and lesser proportion than Li). XRF mapping revealed non-uniform Ce emission center distributions, with highest intensities in green (Figs. 4A and 5A). Mn distribution persisted in both XRF mappings (Figs. 4B and 5B), showing improved uniformity in samples with higher Ce content.

The 2D hyperspectral mapping using total XEOL as contrast showed greater non-uniformity in the distribution of emission centers compared to Li-only samples, with reduced peak broadening at 590 nm. The XEOL spectrum (Fig. 4) revealed distinct patterns in different regions: consistent patterns between points 1–25, 26–28, 29–35, 36–37 and 37–44, 45. The points 26, 29 and 36 present the larger broadening of the peak. The 392 nm peak showed enhanced emission intensity at specific points.

In samples with higher Ce:Li ratios (Fig. 5), the 392 nm peak profile remained consistent across the 2D hyperspectral mapping, with distinct profile for different regions at 590 nm for points 1–4, 5–14, 15–47, and 48. Both Ce-containing samples exhibited selective peak broadening and a potential shoulder near 700 nm.

For Ce-only samples, XRF mapping showed non-uniform Ce and Mn spatial distribution (Fig. 6A and B). The 2D hyperspectral mapping using total XEOL as contrast revealed irregular particle distribution with profiles distinctly different from Li-only and Ce/Li co-doped samples. Horizontal line scan analysis showed distinct 590 nm peak profiles across regions: consistent peaks between points 1–4, 5–12, 13–39, 40–42, with peak broadening and slight wavelength extension at points 43–44. The 764 nm peak appeared better defined compared to Li-containing samples' shoulder characteristic, while the 392 nm peak showed varied regional profiles with enhanced emission intensity relative to Li-containing samples.

3.3. X-ray photoelectron spectroscopy

Fig. 7 shows the XPS spectrum of the Ce 3d binding energy region (880–930 eV) for the $MgB_4O_7{:}Ce_{1wt\%}$ sample. The open black dots represent the raw data after Shirley background subtraction, while the black line denotes a smoothed data curve. Due to the limited statistics, chemical analysis and peak fitting could not be performed using the CasaXPS software (version 2.3.26PR1.0) [23]. However, the results suggest that some Ce^{4+} was reduced to Ce^{3+} during synthesis, as indicated by the difference in peak heights. Specifically, the isolated Ce^{4+} peak around 917 eV, commonly referred to as U^{III}, shows a notable difference compared to the other Ce peaks at binding energies of 885 and 907 eV, commonly referred to as V and V^{III}, respectively. Literature reports of XPS spectra for cerium oxides and mixed cerium oxides show that the height difference between U^{III} and V^{III} typically ranges from approximately 1.5 to 1.7 [24,25]. In our data, this ratio is approximately three, suggesting that roughly 50% of the Ce^{4+} was reduced to Ce^{3+}. Further measurements are necessary to accurately quantify the total amounts of Ce^{4+} and Ce^{3+} in the samples.

3.4. Thermoluminescence

The thermoluminescence spectra are shown in Fig. 8 for the $MgB_4O_7{:}Ce_{1.0wt\%}$ (8a), $MgB_4O_7{:}Ce_{0.33wt\%}Li_{0.67wt\%}$ (8b), and $MgB_4O_7{:}Ce_{0.67wt\%}Li_{0.33wt\%}$ (8c). In all cases, the most prominent emission can be approximated within the range of 550 to 650 nm. While the intensity varies depending on the proportion of dopant and co-dopant used, it is worth noting that the presence of lithium (Li) results in emissions over a broader temperature range. Based on this observation, a simple and well-founded hypothesis is that the emissions from Li-codoped samples are associated with lower activation energy levels, compared to the sample without this ion. This change is associated with the impact of the Li ions on the defect structure of the compound. One possible mechanism involves the influence of Li on the characteristics of other

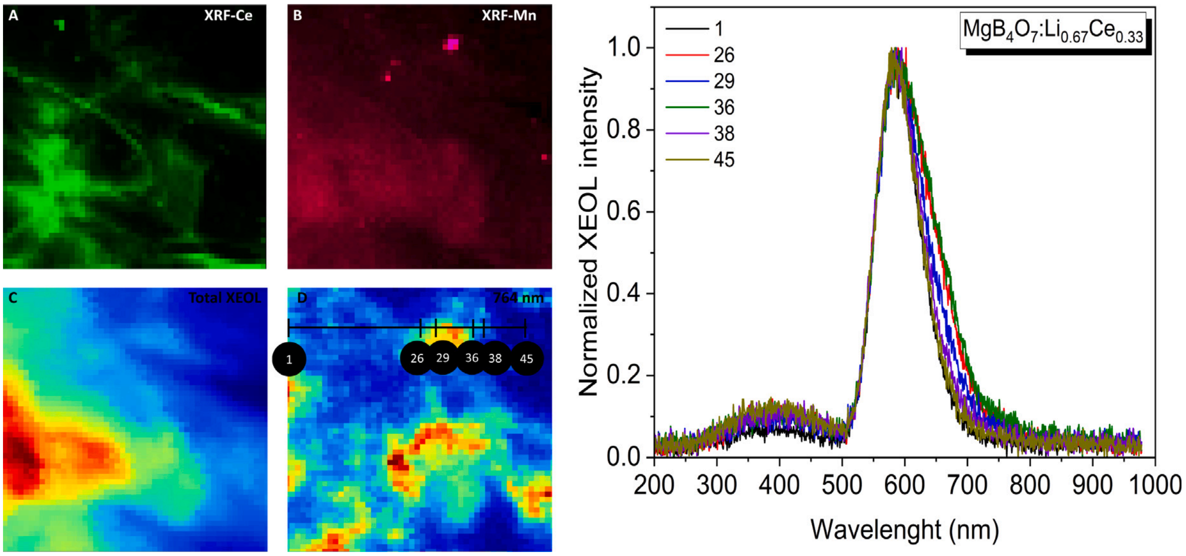

Fig. 4. Correlative XRF and XEOL acquisition in MgB_4O_7:$Li_{0.67}$,$Ce_{0.33}$: XRF mapping obtained using the (a) Ce L_2 and (b) Mn K_α and Ce L_α emission lines. 2D XEOL mapping (c) Total; (d) At 764 nm. XEOL spectrum excited at 9725 eV showed in the right-side. (For interpretation of the references to color in this figure legend, the reader is referred to the web version of this article.)

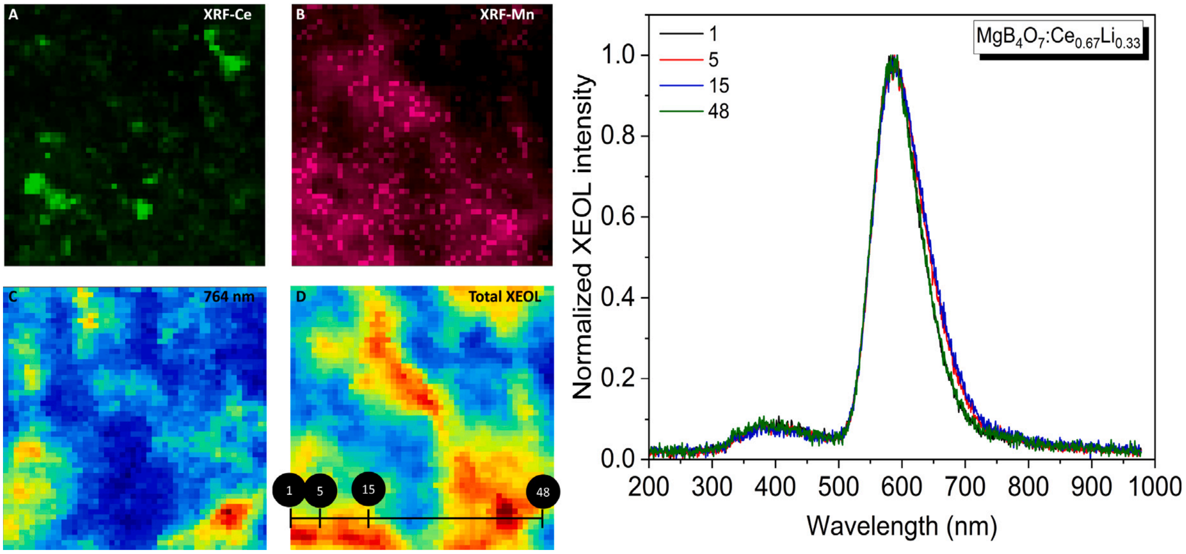

Fig. 5. Correlative XRF and XEOL acquisition in MgB_4O_7:$Ce_{0.67}$,$Li_{0.33}$: XRF mapping obtained using the (a) Ce L_2 and (b) Mn K_α and Ce L_α emission lines. 2D XEOL mapping (c) At 764 nm; (d) Total. XEOL spectrum excited at 9725 eV showed in the right-side. (For interpretation of the references to color in this figure legend, the reader is referred to the web version of this article.)

ions present in the matrix, such as the Ce dopant, which in turn has characteristics such as the valence state influenced by the chemical environment and the precursor used.

4. Discussion

The results obtained from the measurements of Li amounts (Table 1) demonstrated that most of the Li remains in the material during synthesis. Other studies have also shown that in Li-doped materials synthesized at temperatures around 900 °C, most of the Li is incorporated into the matrix, with only a small amount being lost during synthesis [26].

Some studies suggest that in MgB_4O_7:Ce,Li, the concentration of Li in the final product is significantly lower than the amount added to the initial solution, as the optimal Li doping concentration is higher than that of the Ce dopant, and no additional Li-containing phase is observed in the XRD analysis [5,10,13]. In these studies, the optimal Li concentration was approximately 10 mol% for a Ce concentration of 0.3 mol%. When converted, these concentrations correspond to approximately 0.39 wt% of Li and 0.24 wt% of Ce. A similar result was reported by Souza et al. [11] for this type of material, indicating an optimal Li concentration of approximately 0.5 wt% for a Ce concentration of 0.5 wt%.

The fact that no additional Li phase is observed in the material is related to the limited sensitivity of XRD in identifying phases at very low concentrations (<5 wt%) and should not be considered evidence of Li loss. On the other hand, the fact that the optimal Li concentration, in terms of mol %, is significantly higher than that of Ce should not be interpreted as an indication of Li loss during the synthesis process. Instead, it suggests that Li may be acting not only as a charge compensator for the substitution of Mg^{2+} by Ce^{3+} in MgB_4O_7:Ce,Li, but also incorporating defects that could contribute to the enhancement of thermally and optically stimulated luminescence in this material.

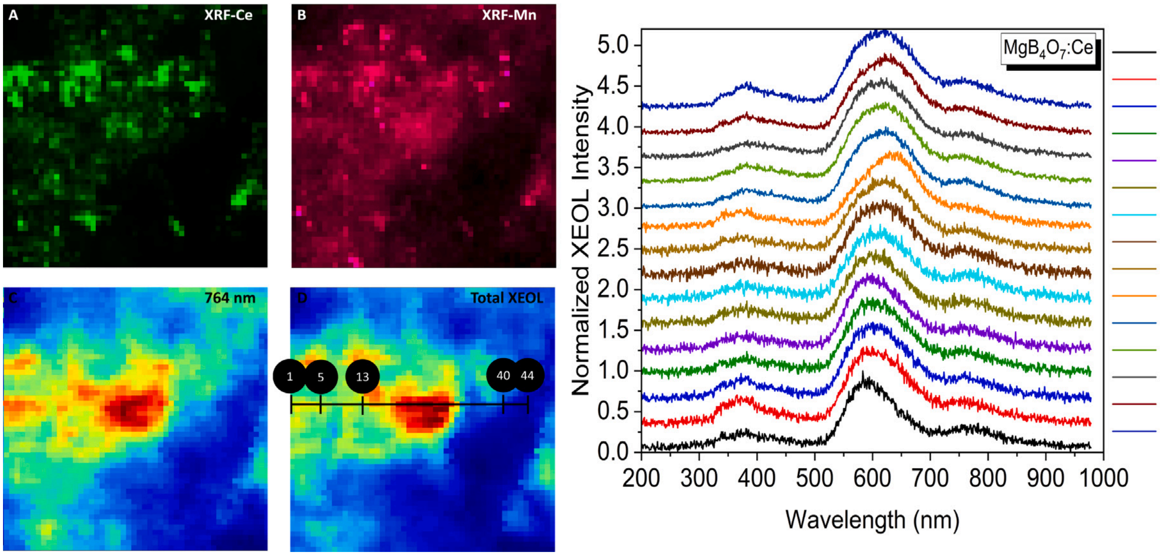

Fig. 6. Correlative XRF and XEOL acquisition in MgB$_4$O$_7$:Ce: XRF mapping obtained using the (a) Ce L$_2$ and (b) Mn K$_\alpha$ and Ce L$_\alpha$ emission lines. 2D XEOL mapping (c) At 764 nm; (d) Total. XEOL spectrum excited at 9725 eV showed in the right-side.

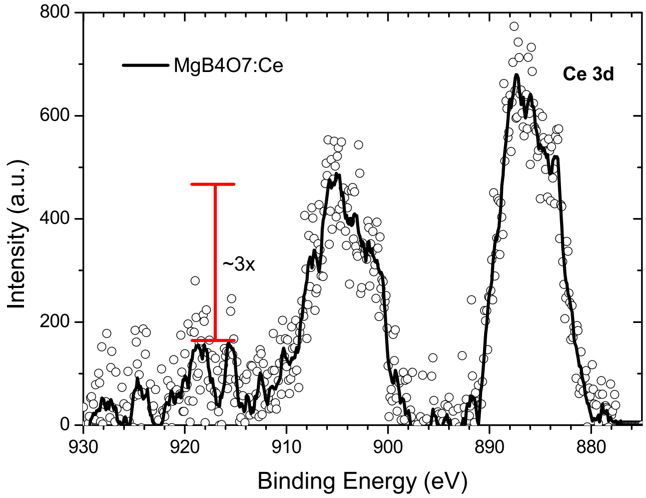

Fig. 7. XPS spectrum of the Ce 3d binding energy region (880–930 eV) for the MgB$_4$O$_7$:Ce sample. The open black dots represent the raw data after Shirley background subtraction, while the black line denotes a smoothed curve of the data.

Another important aspect to be considered is the presence of Ce^{4+} in Ce-doped MgB$_4$O$_7$, since both Ce^{3+} ([Xe]4f^1) and Ce^{4+} ([Xe]4f^0) oxidation states are prevalent in many Ce-based materials due to the facile redox conversion Ce^{3+} ↔ Ce^{4+} [27–29]. In inorganic materials, the predominance of one oxidation state over the other depends on the chemical environment of the site occupied by Ce, as well as the synthesis conditions [27,29].

In this study, we synthesized Ce-MgB$_4$O$_7$ using CeO$_2$ – a non-stoichiometric oxide containing both Ce^{4+} and Ce^{3+} – as the Ce source under an air atmosphere. Our XPS measurements (Fig. 7) indicate that approximately 50% of Ce^{4+} was reduced to Ce^{3+}, demonstrating that Ce^{4+} reduction occurred at the material's surface through electron transfer from neighboring oxygen vacancies to the empty 4f orbital of Ce^{4+} [27–29].

Since XPS is a surface-sensitive analysis technique, it is not possible to confirm whether the same proportion of Ce oxidation states throughout the bulk of the material. To investigate the chemical composition in deeper regions, complementary techniques such as X-ray absorption spectroscopy (XAS) would be required. Relevant to this point, Plokhikh et al. [14] prepared two series of samples of MgB$_4$O$_7$:Ce (0.3 mol%), Li (10 mol%) by solid-state synthesis, using different cerium sources for each series: cerium (IV) oxide and cerium (III) nitrate. In both series, X-ray absorption spectroscopy (XAS) measurements revealed the presence of both Ce^{3+} and Ce^{4+}, with an estimated fraction of 32% Ce^{3+} in the sample synthesized from CeO$_2$ and 74% Ce^{3+} in the sample synthesized from Ce(NO$_3$)$_3$.

These results also suggest that the enhanced TL and OSL signals observed in co-doping with Li in molar excess relative to the Ce dopant extends beyond simple charge compensation of Ce^{3+}, indicating the involvement of additional underlying mechanisms. When Mg^{2+} is substituted by Ce^{4+}, the need for Li as a charge compensator is reduced, since each Ce^{4+} ion can effectively replace two Mg^{2+} ions in the host matrix.

The synthesis conditions prove critical, with subtle variations in chemical environment dramatically influencing oxidation state distribution and subsequent luminescence mechanisms. Theoretical studies indicate that, in undoped MgB$_4$O$_7$, the most probable defects are directly (as in Frenkel defects) or indirectly (as in anti-Schottky defects) related to oxygen vacancies (F^0, F^+, and F^{2+} centers) and interstitial O^{2-} ions [4,30]. Measurements performed using Electron Paramagnetic Resonance (EPR) provide experimental evidence for the existence of F^+ centers in these materials and their relationship with the TL signal in doped MgB$_4$O$_7$ [31,32]. Thus, it is likely that the luminescence signals at 360 nm and 550 nm observed in undoped MgB$_4$O$_7$, both after thermal stimulation of irradiated samples (TL) and directly under the action of ionizing radiation (RL), are related to radiative recombination processes involving F-centers (emissions from F^0 and F^+ centers) and/or due to radiative recombination of self-trapped exciton electron–hole pairs [33,34].

According to Kalinkin et al. [34], the emission at approximately 360 nm, attributed to self-trapped excitons and observed in MgB$_4$O$_7$-based materials, occurs exclusively during the irradiation process and does not result from the thermal stimulation of the irradiated tetraborate. In other words, this signal is not associated with energy storage. Specifically, the emission around 550 nm, observed in both undoped MgB$_4$O$_7$ materials and those doped with rare earth elements, was associated by Kalinkin et al. [34] with the recombination of electrons with F^{2+} centers.

In the case of MgB$_4$O$_7$ doped solely with Li, theoretical studies have shown that Li$^+$ ions are preferentially incorporated at the Mg^{2+} site, compensated by $\mathrm{Mg}_i^{\bullet\bullet}$ in the interstitial pores of the material

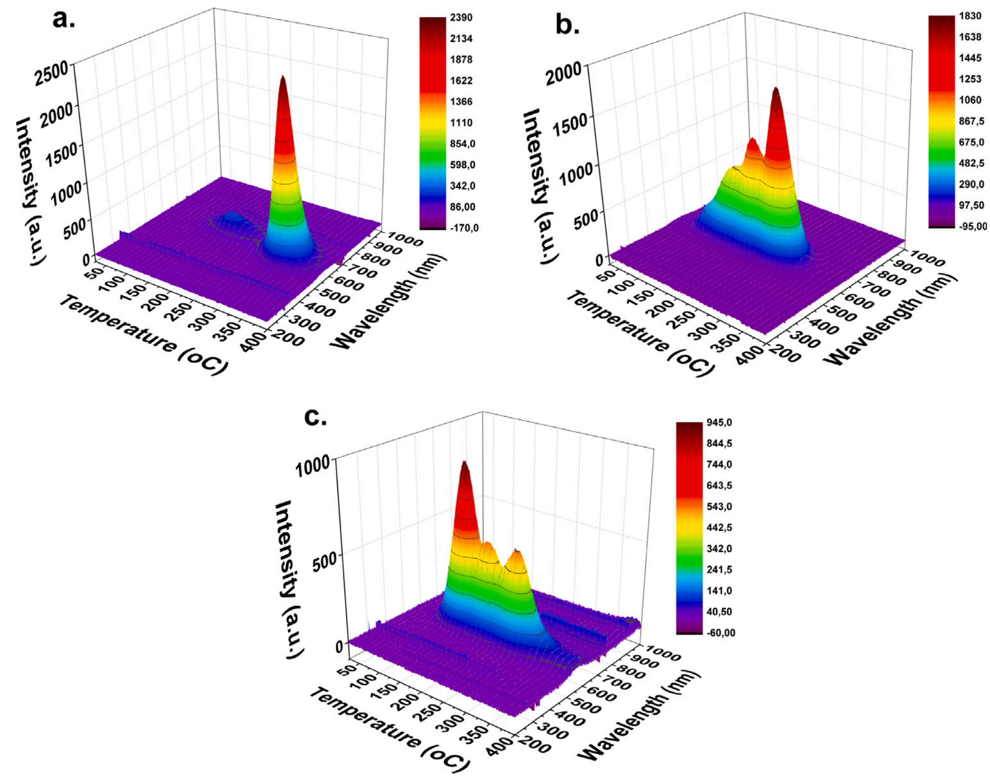

Fig. 8. TL emission spectra as a function of temperature and wavelength, obtained for the (a) MgB_4O_7:$Ce_{1.0wt\%}$, (b) MgB_4O_7:$Ce_{0.33wt\%}Li_{0.67wt\%}$, and (c) MgB_4O_7:$Ce_{0.67wt\%}Li_{0.33wt\%}$.

$(2\mathrm{Li}'_{\mathrm{Mg}}\mathrm{Mg}_i^{\bullet\bullet})$ [12]. Considering the formation of this type of defect in MgB_4O_7 doped with Li, as discussed in detail by [12], it is expected that Li interacts with surface F^0 and F^+ centers, promoting the formation of F^{2+} centers. Thus, in this material, electronic recombinations would predominantly occur at F^{2+} centers ($F^+ + \mathrm{h}^+$) formed upon irradiation of the material, and TL emissions would be associated with the excited state F^{+*} ($F^{2+} + e^- \rightarrow [F^+]^* \rightarrow F^+ + h\nu$), rather than the excited state F^{0*} ($F^+ + e^- \rightarrow [F^0]^* \rightarrow F^0 + h\nu$). In this case, the electron traps would be predominantly the F^{2+} centers formed by the introduction of Li into the material ($F^{2+} + e^- \rightarrow F^+$), and the TL emission should be observed at lower temperatures because they are shallow traps. In various materials, F^{2+} centers are closer to the conduction band, potentially acting as shallow electron traps, while F^0 and F^+ centers are positioned at deeper levels [35–38]. Therefore, Li doping of MgB_4O_7 is expected to suppress the intrinsic TL signal observed in pure MgB_4O_7 at higher temperatures, while preserving the TL signal at lower temperatures. This behavior can be observed in the TL spectra presented by Batista et al. [12] for pure MgB_4O_7 and Li-doped MgB_4O_7.

In many materials, the photons emitted from F^{+*} centers have higher energy than those emitted from F^{0*} centers [39]. The emissions associated with both F-centers typically occur in the range of 300 to 600 nm [39]. Borate materials exhibit emissions in the 520–600 nm range that are attributed to electron recombinations in oxygen vacancies with trapped holes (V_O^{++} and V_O^{+}) [40,41]. This would explain why the MgB_4O_7 materials doped only with Li, as well as those doped with Ce and co-doped with Li, exhibited similar XEOL spectra (Figs. 3, 4, 5, and 6), with a broad main band between 500 and 700 nm, which we are attributing to the predominance of emissions from F^{+*}. Thus, we agree with Kalinkin et al. [34] in attributing the emission at approximately 580 nm in undoped MgB_4O_7 to F^{+*} centers.

MgB_4O_7 doped exclusively with Ce showed a XEOL spectrum with a broad main band in the 500–700 nm region, accompanied by a shoulder at 750 nm. The deconvolution (see Fig. A.10) of this band and shoulder shows three peaks with maxima at approximately 580 nm, 640 nm and 750 nm that may be associated with the emission of F^{+*}, F^{0*} and clusters of F-centers (e.g. F_2 and F_2^+), respectively. The emission band at 750 nm was observed by Altunal et al. [42] in radioluminescence (RL) measurements on undoped MgB_4O_7, and the authors attributed it to oxygen defects in the material structure. In the material doped or co-doped with Li, the emissions associated with the F^{0*} centers and clusters of F-centers are no longer clearly observed, because in the doping with Li the F^+ centers predominate in the material (see the XEOL spectra).

In MgB_4O_7 doped with Ce, considering that the synthesis methods involve thermal treatment in an air atmosphere, Ce^{3+} and Ce^{4+} coexist in equilibrium, with their relative ratios depending on the synthesis conditions and the precursor reagents used as the Ce source. The presence of Ce^{3+}/Ce^{4+} sites makes the mechanisms behind the luminescence observed in the material highly complex. Generally, it is expected that during material irradiation, holes are captured by Ce^{3+} sites, converting them to Ce^{4+}, while electrons are trapped at various sites. Upon thermal or optical stimulation, the trapped electrons are released and recombine with the holes, converting Ce^{4+} back into Ce^{3+}, but in an excited state. The relaxation of this excited state is responsible for the typical (5d → 4f) transition emission of Ce^{3+}. EPR data provide evidence for the formation of BO_3^{2-} radicals in MgB_4O_7 upon irradiation, attributed to the trapping of holes by BO_3^{3-} ions [32,43]. Notwithstanding, the complete thermal decomposition of these radical species at temperatures exceeding 150 °C effectively eliminates their contribution as recombination centers for the TL peaks observed in MgB_4O_7:Ce, the emissions of which are observed above 200 °C.

Charge transfer luminescence involving Ce^{4+} is also possible [44–46]. In this process, after material irradiation, an electron from a neighboring O^{2-} ion is transferred to Ce^{4+}, temporarily converting it into Ce^{3+}. The system momentarily stabilizes with Ce^{3+} and O^- (O^{2-} + h^+), forming an excited complex. Subsequently, the electron in Ce^{3+} returns to oxygen, restoring Ce^{4+} and O^{2-}. During this return to the ground state, light emission occurs. Furthermore, charge transfer processes can involve the transfer of electrons from neighboring F-centers (F^0 or F^+) to Ce^{4+}, also temporarily converting it into Ce^{3+}. In this case, the system stabilizes in an excited complex formed by Ce^{3+} and F^+ ($F^0 + h^+$) or F^{2+} ($F^+ + h^+$). Subsequently, the electron in Ce^{3+} returns to the F^+ or F^{2+} center, restoring Ce^{4+} and emitting light.

The TL spectrum of Ce-doped MgB_4O_7 reported in the scientific literature exhibits emissions exclusively at 580 nm, while the PL spectra (λ_{ex} = 318 nm) reveal emissions only around 350 nm, attributed to the $5d \rightarrow 4f$ transitions of Ce^{3+} ions [6,47,48]. The absence of $5d \rightarrow 4f$ transitions in the TL spectrum of MgB_4O_7 doped with Ce suggests that the TL emission at 580 nm is more likely associated with the F-centers of the host matrix. This hypothesis is supported by the fact that the same TL emission is observed in materials doped with other elements, such as gadolinium, which does not exhibit luminescence in this spectral range [49]. The analysis of the XRF and XEOL maps of MgB_4O_7:Ce (Fig. 6) demonstrates that the regions of maximum optical emission intensity (XEOL) do not coincide with the regions of highest XRF emission intensity attributed to Ce. These results provide further evidence of a predominant association between the observed TL emissions and F-centers.

In the XEOL spectrum of the Ce-doped MgB_4O_7 sample (Fig. 6), a broad emission band is observed in the range of 300 to 400 nm, with two distinct peaks centered at 346 nm and 371 nm. The emissions at 346 nm and 371 nm can be associated with $5d \rightarrow 4f$ transitions of the Ce^{3+} ion. The energy difference between the peaks is 1947 cm^{-1}. It is well known that the Ce^{3+} emission band exhibits a doublet structure due to the spin–orbit splitting of the ground state ($^2F_{7/2}$ and $^2F_{5/2}$), with an energy difference of approximately 2000 cm^{-1} [50]. This energy difference is nearly independent of the host lattice, as the 4f shell is effectively shielded by the outer $5s^25p^6$ shell. In Ce-doped MgB_4O_7, the two emission peaks corresponding to transitions from the lowest lying 5d level to the $^2F_{5/2}$ and $^2F_{7/2}$ levels of the ground state configuration are seen at 340 nm and 363 nm [10]. Additionally, as previously noted in this section, the XEOL spectrum shows a broad band between 550 and 700 nm, with a maximum around 640 nm and a shoulder at 750 nm, which are likely related to emissions from F-centers in the material.

In Ce-doped MgB_4O_7, the emissions may be associated with the following mechanisms, which appear highly probable and may occur simultaneously:

(I) Emissions involving the Ce^{3+} ion and F-centers:

Material exposure to Ionizing Radiation (IR):

$$Material + IR \rightarrow nh^+ + ne^-, n = a + b$$

$$Hole\ trapping\ by\ Ce^{3+};$$

$$nCe^{3+} + nh^+ \rightarrow nCe^{4+}$$

$$Electron\ trapping\ by\ F^+\ and\ F^{2+}\ centers;$$

$$aF^{2+} + ae^- \rightarrow aF^+$$
$$bF^+ + be^- \rightarrow bF^0$$

During thermal or optical stimulation:

$$Electron\ detrapping\ by\ thermal\ (or\ optical)\ energy\ (E_T);$$

$$aF^+ + bF^0 + E_T \rightarrow aF^{2+} + bF^+ + ne^-$$

$$Electron - hole\ recombination\ and\ light\ emission;$$

$$nCe^{4+} + ne^- \rightarrow n[Ce^{3+}]^* \rightarrow nCe^{3+} + Light\ (300 - 400\ \text{nm})$$

(II) Emissions involving both Ce^{3+} and Ce^{4+} ions:

Exposure to Ionizing Radiation (IR):

$$Material + IR \rightarrow nh^+ + ne^-$$

$$Hole\ trapping\ by\ Ce^{3+}$$

$$nCe^{3+} + nh^+ \rightarrow nCe^{4+}$$

$$Electron\ trapping\ by\ Ce^{4+}$$

$$nCe^{4+} + ne^- \rightarrow nCe^{3+}$$

During thermal or optical stimulation:

$$Electron\ detrapping\ by\ thermal\ (or\ optical)\ energy\ (E_T);$$

$$nCe^{3+} + E_T \rightarrow nCe^{4+} + ne^-$$

$$Electron - hole\ recombination\ and\ light\ emission;$$

$$nCe^{4+} + ne^- \rightarrow n[Ce^{3+}]^* \rightarrow nCe^{3+} + Light\ (300 - 400\ \text{nm})$$

(III) Emissions involving Ce^{4+} ions and F-centers:

Exposure to Ionizing Radiation (IR):

$$Material + IR \rightarrow nh^+ + ne^-, n = a + b$$

$$Hole\ trapping\ by\ F^0\ and\ F^+\ centers;$$

$$aF^0 + ah^+ \rightarrow aF^+$$
$$bF^+ + bh^+ \rightarrow bF^{2+}$$

$$Electron\ trapping\ by\ Ce^{4+};$$

$$nCe^{4+} + ne^- \rightarrow nCe^{3+}$$

During thermal or optical stimulation:

$$Electron\ detrapping\ by\ thermal\ (or\ optical)\ energy\ (E_T);$$

$$nCe^{3+} + E_T \rightarrow nCe^{4+} + ne^-$$

$$Electron - hole\ recombination\ and\ light\ emission;$$

$$aF^+ + bF^{2+} + ne^- \rightarrow a[F^0]^* + b[F^+]^* \ldots$$

$$\ldots \rightarrow aF^0 + bF^+ + Ligth\ (500 - 750\ \text{nm})$$

As can be observed in the TL spectrum of MgB_4O_7 doped with Ce (Fig. 8), as well as in the TL spectrum reported by Yukihara et al. [6] for this type of material, the only thermoluminescent emission detected occurs at 580 nm. This indicates that, in Ce-doped MgB_4O_7, TL emissions are primarily associated with F-centers. In this context, Ce^{4+} ions present in the material act as electron traps via mechanism III, being released by detrapping at approximately 300 °C, depending on the heating rate of the material. The observation of characteristic Ce^{3+} emissions in the XEOL spectrum (Fig. 6) and PL spectra (Fig. 9), but not in the TL spectrum (Fig. 8) of MgB_4O_7:Ce, suggests that Ce^{3+} ions do not act as energy storage centers during the irradiation process. A possible explanation is the predominance of F^0 centers in the unirradiated material, compared to F^+ and F^{2+} centers. It is assumed that these F-centers effectively compete with Ce^{3+} ions for hole trapping during irradiation of the material, which disfavors TL emissions through mechanisms I and II.

The Ce^{4+} acts as electron traps; a higher concentration of Ce^{4+} within the material will favor emissions via mechanism III, and F-center emissions in the 500–750 nm range are likely to be dominant. Conversely, in materials with a higher Ce^{3+} content, which act as hole traps, the dominant emissions will occur at 360 nm, corresponding to the $5d \rightarrow 4f$ transitions of this ion. This hypothesis can be confirmed in the work of Plokhikh et al. [14], who produced Ce-doped MgB_4O_7 using CeO_2, obtaining a material with a higher amount of Ce^{4+} (68%) compared to Ce^{3+} (32%) and a pronounced TL emission centered at 580 nm, detected at 250 °C (rate 1 °C/s). On the other hand, when producing Ce-doped MgB_4O_7 using $Ce(NO_3)_3$, the authors obtained a material with a predominance of Ce^{3+} (74%) compared to Ce^{4+} (26%), detecting at 250 °C (rate 1 °C/s) a TL emission predominantly centered at 380 nm.

Since Ce^{4+} has an ionic radius very close to that of Mg^{2+}, it is likely that, in the doping of MgB_4O_7 with Ce^{4+}, Ce^{4+} will substitute Mg^{2+}.

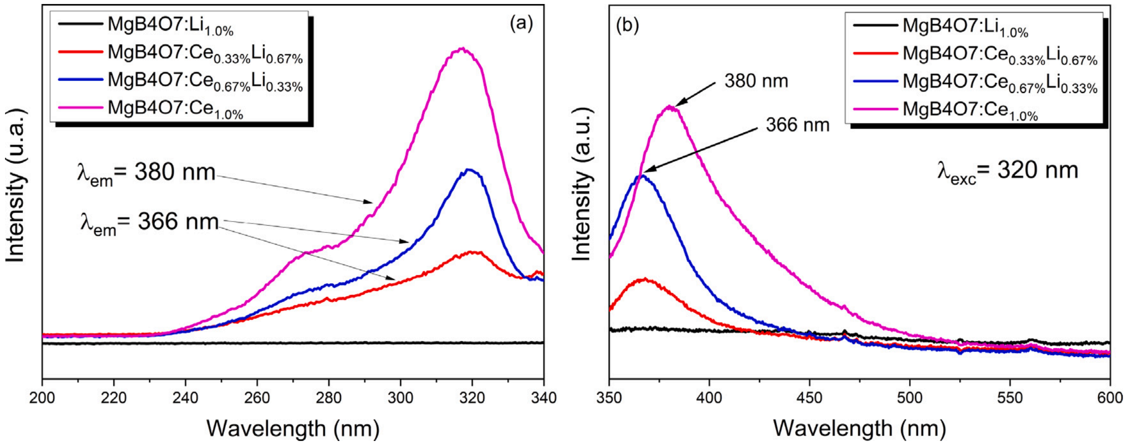

Fig. 9. (a) Excitation and (b) emission photoluminescence spectra of MgB_4O_7 doped and co-doped with Ce and Li.

To compensate for the charge, a Mg^{2+} vacancy with two electrons will be created. In this scenario, the reduction of Ce^{4+} to Ce^{3+} could occur through charge transfer from neighboring oxygen vacancies containing electrons, as seen in CeO_2 and other Ce-doped materials [51–56]. The experimental conditions employed in this study likely favored the reduction of Ce^{4+} in Ce-MgB4O7, as indicated by the XPS data, which revealed the predominance of Ce^{4+}, at least in the surface region of the material. This reduction was likely driven by electron transfer from neighboring oxygen vacancies, leading to the formation of stable $Ce^{3+}-V_o$ complexes [51–54]. The reduction processes can be described by the following reactions: $(Ce^{4+}-F^0) \rightarrow (Ce^{3+}-F^+)$ and $(Ce^{4+}-F^+) \rightarrow (Ce^{3+} - F^{2+})$.

The lattice energy of MgB_4O_7 is very high (−466.399 eV), making the formation of structural defects less favorable [4]. However, once defects are formed, such as oxygen vacancies, they can be efficiently stabilized through charge interactions. These interactions tend to favor electron capture by the vacancies, leading to a higher formation of F^0 centers rather than F^+ centers [45]. Additionally, F^0 centers are more likely to transfer an electron to Ce^{4+} than F^+ centers. As a result, in the MgB_4O_7 doped with Ce used in this study, the formation of the $Ce^{3+} - F^+$ complex is the most probable. In this case, the TL emission will occur via a modified mechanism I, which takes place concomitantly with mechanisms II and III. In the modified mechanism I, the hole trap will not be the isolated Ce^{3+} ion, but rather the $Ce^{3+}-F^+$ complex. Since the F^+ center is an anionic defect, the hole will be preferentially trapped at the F^+ center, rather than at the Ce^{3+}. A plausible mechanism for TL emission involving these complexes would be:

Emissions involving the Ce^{3+} - F^+ complex and F-centers:

Exposure to Ionizing Radiation (IR):

$$Material + IR \rightarrow nh^+ + ne^-, n = a + b$$

Hole trapping by Ce^{3+};

$$n(Ce^{3+} - F^+) + nh^+ \rightarrow n(Ce^{3+} - F^{2+})$$

Electron trapping by F^+ *and* F^{2+} *centers*;

$$aF^{2+} + ae^- \rightarrow aF^+$$
$$bF^+ + be^- \rightarrow bF^0$$

During thermal or optical stimulation:

Electron detrapping by thermal (or optical) energy (E_T);

$$aF^+ + bF^0 + E_T \rightarrow aF^{2+} + bF^+ + ne^-$$

Electron – hole recombination and light emission;

$$n(Ce^{3+}-F^{2+})+ne^- \rightarrow n(Ce^{3+}-F^{+*}) \rightarrow n(Ce^{3+} - F^+)+ Light(500-750 \text{ nm})$$

A relevant aspect to consider is the effect of Li co-doping on the thermoluminescence of Ce-doped MgB_4O_7. Based on the discussion presented at the beginning of this section, in Ce-doped MgB_4O_7, co-doping with Li is expected to promote the formation of F^{2+} centers and reduce the quantity of F^0 and F^+ centers. Considering mechanisms I, II, and III, the introduction of Li in Ce-doped MgB_4O_7 would likely enhance the TL signal mainly through mechanism I, due to the increased number of electron traps represented by F^{2+} centers. On the other hand, the reduction of F^0 and F^+ centers would decrease the TL emission via mechanism III, as these centers are associated with recombination sites.

It is known that F^{2+} centers act as shallow traps, resulting in TL emissions at lower temperatures. This effect is clearly evidenced in the work of [14], who compared the TL spectrum of MgB_4O_7 doped with 0.3% Ce, exhibiting a single peak at approximately 275 °C (heating rate of 5 °C/s), with the same material co-doped with 10% Li, which exhibits additional peaks below 150 °C. In our study, we observed similar behavior (Fig. 8). The MgB_4O_7 sample doped with 1% Ce exhibits an intense TL peak at 326 °C (heating rate of 10 °C/s). In contrast, the Li co-doped samples demonstrate the arising of TL peaks at lower temperatures, below 250 °C, evidencing the influence of Li on the formation of shallower traps.

Thus, in Ce-doped MgB_4O_7, where the concentration of Ce^{3+} is higher than that of Ce^{4+}, it is expected that an increase in the Li concentration will lead to a significant enhancement of emissions at 390 nm, via mechanism I, and a reduction of emissions near 580 nm due to the inhibition of mechanism III. Li co-doping induces the formation of F^+ and F^{2+} centers (electron traps), enhancing Ce^{3+} emissions (hole traps) and suppressing F^0 center emissions. It is believed that lithium promotes the conversion of F^0 centers into F^+ and F^{2+}, reducing hole competition with Ce^{3+} and intensifying its emissions. This reasoning seems plausible, especially when compared with experimental data. In an experimental study, Yukihara et al. [6] observed that in the TL signal detected at 250 °C (with a heating rate of 1 °C/s), the increase in Li content in Ce-doped MgB_4O_7 samples resulted in an increase in the emission at 380 nm and a reduction in the emission at 580 nm. The materials studied were produced using $Ce(NO_3)_3$ as the Ce precursor, so the material is expected to contain a higher amount of Ce^{3+} than Ce^{4+}.

In materials with a higher concentration of Ce^{4+}, increasing the Li content is not expected to significantly enhance the TL signal via mechanism I when compared to a material with a higher Ce^{3+} concentration, due to the limited amount of Ce^{3+} available. Additionally, the TL signal via mechanism III would also be reduced due to the decrease in the population of F^0. Although the population of F^0 centers (hole traps) decreases due to Li doping, the population of $F+$ centers may not change significantly. This is because the F^+ centers generated from the conversion of F^0 centers can partially or fully compensate for those converted to F^{2+} centers. As a result of the increase in the F^{2+} population (electron traps) and the suppression of the F^0 population (hole traps), the F^+ centers will start to act primarily as hole traps, leaving only Ce^{4+} as deep electron traps. In the case of this type of material, Li doping is expected to reduce the intensities of the TL peaks at high temperatures due to the decrease in deep electron traps of the F^+ type.

On the other hand, the increase in the F^{2+} population due to co-doping with Li, combined with the limited content of Ce^{3+}, may cause the F^{2+} centers to not only contribute to mechanism I but also play a role in emission through an alternative mechanism, which will be presented below. This mechanism is expected to occur simultaneously with mechanisms I, II, and III.

Exposure to Ionizing Radiation (IR):

$$Material + IR \rightarrow nh^+ + ne^-$$

$$Hole\ trapping\ by\ F^+;$$

$$nF^+ + nh^+ \rightarrow nF^{2+}$$

$$Electron\ trapping\ by\ F^{2+};$$

$$nF^{2+} + ne^- \rightarrow nF^+$$

During thermal or optical stimulation:

$$Electron\ detrapping\ by\ thermal\ (or\ optical)\ energy\ (E_T);$$

$$nF^+ + E_T \rightarrow nF^{2+} + ne^-$$

$$Electron - hole\ recombination\ and\ light\ emission;$$

$$nF^{2+} + ne^- \rightarrow n[F^+]^* \rightarrow nF^+ + Ligth\ (500 - 750\ \text{nm})$$

The F^{2+} centers do not have localized electrons and do not possess occupied states. Therefore, in many materials, their empty states are positioned near the conduction band [35–38]. As a result, the F^{2+} centers act as shallow electron traps. Through this alternative emission mechanism, electrons trapped in the shallow traps of the F^{2+} centers are recombined with the holes trapped by the deeper F^+ centers.

Thus, in Ce-doped MgB_4O_7, when the Ce^{4+} content is higher than that of Ce^{3+}, or when the concentration of the $Ce^{3+} - F^+$ complex is higher than that of Ce^{4+}, Li co-doping is not expected to alter the TL emission wavelengths, which should remain between 550 and 700 nm. However, co-doping with Li should suppress the emissions at 640 nm and 750 nm, attributed to the F^0 centers and the F_2 cluster (F^0+F^0), respectively, and should not alter the TL emission at 580 nm (attributed to the F^+ centers), as can be observed in the XEOL spectrum (see the XEOL spectra). In this scenario, in materials where the concentration of Ce^{4+} is higher than that of Ce^{3+}, TL emissions are predominantly associated with mechanism III and the previously described alternative mechanism. On the other hand, in materials with a higher amount of the $Ce^{3+} - F^+$ complex than Ce^{4+}, TL emission is primarily linked to the modified mechanism I and the alternative mechanism. However, increasing the Li content tends to enhance the TL signal at lower temperatures because of the increase in the number of shallow traps (i.e. F^{2+} center). This trend is evident in the TL spectra presented in Fig. 8, which show emission only at 580 nm and indicate an increase in the TL signal at 150 °C (rate of 10 °C/s) with increasing Li content.

Some authors attribute the TL emission band with a maximum at approximately 580 nm, observed in both rare-earth-doped and undoped MgB_4O_7, to the presence of manganese impurities originating from the magnesium precursor used in the material's synthesis. The Mn^{2+} ion has an ionic radius similar to that of Mg^{2+}, which facilitates its incorporation into the MgB_4O_7 crystal lattice. Moreover, Mn^{2+} exhibits the ${}^4T_1({}^4G) \rightarrow {}^6A_1({}^6S)$ transition, resulting in light emission in the range of 500 to 700 nm, varying from green to near-infrared depending on the type of ligand and coordination symmetry [57]. TL spectra of Mn-doped MgB_4O_7 exhibit an emission centered at 580 nm, with a peak intensity at 360 °C (heating rate of 5 °C/s) [58].

The attribution of the 580 nm emission in MgB_4O_7 samples to Mn^{2+} impurities remains unclear and insufficiently substantiated by experimental evidence. Yukihara et al. [6] attributed the TL emission around 580 nm, observed in MgB_4O_7-based phosphors, to Mn^{2+} contamination from low-purity $Mg(NO_3)_2$ (98%) used as a precursor in synthesis. Specifically, they identified Mn^{2+} as a contaminant present at approximately 2 ppm concentration. This interpretation was later reaffirmed by the experimental study conducted by Gustafson et al. [10].

However, other authors have used high-purity magnesium precursors, such as magnesium nitrate (99.9%), magnesium carbonate (99.9%) and magnesium oxide (99.99%), and still observed TL emission around 580 nm [11,34,42,49,59]. Even assuming that the entire amount of Mn^{2+} present in low-purity $Mg(NO_3)_2$ were incorporated into the MgB_4O_7 crystal lattice, it would correspond to a doping level of approximately $2 \times 10^{-4}\%$ by weight. It is unlikely that Mn^{2+}, at such a low concentration, would be solely responsible for the luminescence signal at 580 nm with the observed intensities in MgB_4O_7 materials. Furthermore, as pointed out by Kalinkin et al. [34] in a recent study, the available EPR data indicate the absence of paramagnetic centers related to Mn in MgB_4O_7, suggesting that this emission may be an intrinsic property of the host lattice rather than a result of manganese contamination.

Another aspect that highlights the inconsistency of this hypothesis is the fact that TL measurements in MgB_4O_7 doped with Ce and Li show emissions attributed to Mn^{2+} with higher intensity than those of Ce^{3+}. However, the photoluminescence emission spectrum of the material, when excited at approximately 320 nm, exhibits only the emission of Ce^{3+}. This behavior is evident in both our PL and TL measurements (Figs. 8 and 9) and in other studies from the literature [11]. If the material contained enough Mn^{2+} to generate TL emissions of such high intensity — exceeding even those of Ce^{3+} — these emissions should also be present in the PL spectrum. This is because many Mn^{2+}-doped materials, including tetraborates, when excited at approximately 320 nm, exhibit strong emissions from this ion at 580 nm [60–64].

As shown in the XRF maps (Figs. 3 to 6), the presence of Mn was detected in all MgB_4O_7 samples doped and co-doped with Ce and Li. However, in a previous study, we showed that the Mn content is at trace levels, with concentrations hundreds of times lower than that of Ce [12]. Therefore, it is unlikely that the emission around 580 nm is associated with Mn. Furthermore, when comparing the XRF and XEOL maps of the samples, Mn is observed to be homogeneously distributed throughout the material. However, there are regions in the XRF map without the presence of Mn, where the corresponding regions in the XEOL map exhibit emission at 580 nm. Additionally, in both the XEOL and XRF maps, the areas with higher Mn concentrations do not clearly correspond to the regions with the highest emission intensities at 580 nm.

It is likely that the broad emission band centered at 580 nm observed in MgB_4O_7-based phosphors is related to radiative recombination processes involving F-centers (F^+ and F^{2+} of the host lattice and/or photoconversion of these centers [34]. In a recent study, Plokhikh [65] observed an increase in the TL signal at 580 nm in MgB_4O_7:Ce,Li materials synthesized at higher annealing temperatures. Although the authors attributed the increase in the TL signal at 580 nm to easier Mn incorporation at higher temperatures, it is more likely that the increase is related to variations in the concentration of oxygen vacancies with increasing annealing temperature [66]. While experimental evidence suggests that F-centers contribute to the emissions of Ce and Li-doped MgB_4O_7, and we have proposed several possible emission mechanisms involving these centers, further experimental and theoretical studies are required to confirm this.

5. Conclusions

Comprehensive characterization was performed using multiple advanced techniques, including nuclear reaction analysis, X-ray photoelectron spectroscopy, synchrotron-based X-ray nanospectroscopy, photoluminescence, and thermoluminescence emission spectra. These analyses provided relevant insights into aspects such as composition, oxidation state, and mechanisms involved in the optical properties of the synthesized materials. The news findings of this study are:

- Nuclear reaction spectra analyses reveal that lithium remains present in the material throughout the synthesis process, with a maximum difference of 11% between the nominal and measured lithium quantities.
- X-ray photoelectron spectroscopy analyses reveal that approximately 50% of Ce^{4+} undergo reduction to Ce^{3+} on the material's surface due to electron transfer from adjacent oxygen vacancies to the empty 4f orbital of Ce^{4+}.
- Correlative imaging analysis of Li and Ce co-doped MgB_4O_7, including X-ray fluorescence and X-ray excited optical luminescence mapping reveal non-uniform Ce emission center distributions.
- XEOL spectra reveal distinct luminescence patterns across different regions of the samples, with a pronounced difference observed in samples containing only cerium.
- The thermoluminescence emission band, with a maximum at approximately 580 nm, is associated with F-center emission rather than emission originating from manganese impurity traces.
- Lithium co-doping tends to enhance the thermoluminescence signal at lower temperatures due to an increase in the number of shallow traps, such as F^{2+} center.
- Mechanisms were proposed to elucidate the emission process involving Ce ions and F-centers.

These results provide novel insights into the synergistic effects of Li and Ce co-doping in MgB4O7, offering new hypotheses about luminescence mechanisms. Our findings contribute to the current understanding by also introducing characterization techniques not commonly seen in this type of discussion, bringing new aspects to the analysis and adding insights toward the development of next-generation luminescent materials with tailored optical properties.

CRediT authorship contribution statement

Jorge L.O. Santos: Writing – review & editing, Writing – original draft, Visualization, Validation, Supervision, Investigation, Formal analysis, Data curation, Conceptualization. **Adelmo S. Souza:** Visualization, Methodology, Investigation, Data curation. **João V.B. Valença:** Writing – original draft, Visualization, Methodology, Investigation, Data curation. **Henrique Trombini:** Writing – original draft, Visualization, Methodology, Investigation, Data curation. **Cláudio Radtke:** Visualization, Methodology, Investigation, Data curation. **Iury S. Silveira:** Visualization, Methodology, Investigation, Data curation. **Roger G. Fernandes:** Writing – original draft, Methodology, Data curation, review. **Heveson Lima:** Writing – review & editing, Writing – original draft, Visualization, Validation, Supervision, Project administration, Investigation, Formal analysis, Data curation, Conceptualization.

Declaration of competing interest

The authors declare that they have no known competing financial interests or personal relationships that could have appeared to influence the work reported in this paper.

Acknowledgments

The authors acknowledge the CNPq, Brazil (N° 310586/2021-6 and 404784/2021-6), CAPES, Brazil, FINEP, Brazil (N° 0553/18), and FAPESB/BA, Brazil (APP0036/2023), Brazilian funding agencies, Brazil, for financial support. The authors would also like to thank Carnaúba/Sirius-LNLS/CNPEM, Brazil (proposal 20241775).

Appendix. STXM, XRF, 2D XEOL mapping, and XEOL spectrum

See Figs. A.10–A.12.

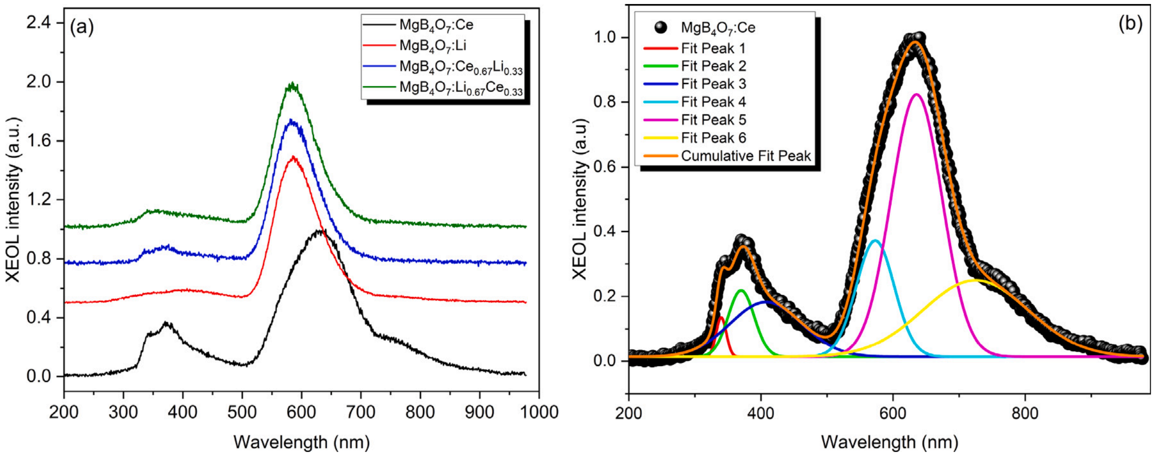

Fig. A.10. (a) XEOL spectra of MgB_4O_7 doped and co-doped with Ce and Li obtained in the center of the particle and b) Deconvolution of the XEOL spectrum of Ce-doped MgB_4O_7.

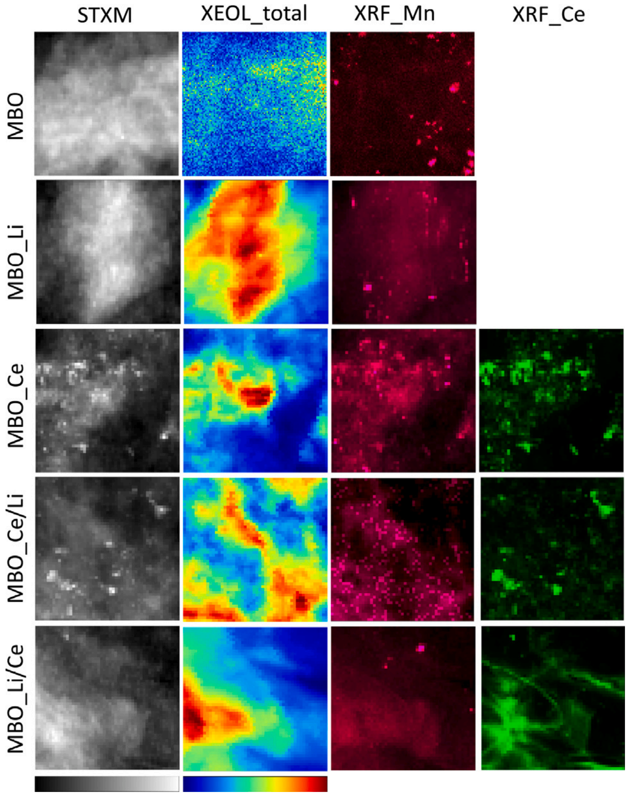

Fig. A.11. Multimodal characterization of MgB_4O_7 samples with different dopant configurations (Ce-doped, Li-doped, and Ce/Li co-doped) using complementary techniques: Scanning Transmission X-ray Microscopy (STXM) for morphological features, X-ray Fluorescence (XRF) mapping of Ce and Mn distributions, and total X-ray Excited Optical Luminescence (XEOL) for emission properties. The STXM images reveal structural variations across samples, while the element-specific XRF maps demonstrate the spatial distribution of Ce activator ions and Mn impurities. The corresponding XEOL maps highlight the enhanced luminescence efficiency in the Ce/Li co-doped sample, indicating successful modification of the host lattice environment by Li co-doping to optimize Ce^{3+} emission centers. This correlative microscopic approach provides insight into the relationship between dopant distribution and resulting luminescence properties in these phosphor materials.MBO = MgB_4O_7 is the pure matrix. MBO-Ce/Li = MgB_4O_7:$Ce_{0.67}Li_{0.33}$ and MBO-Li/Ce = MgB_4O_7:$Ce_{0.33}Li_{0.67}$.

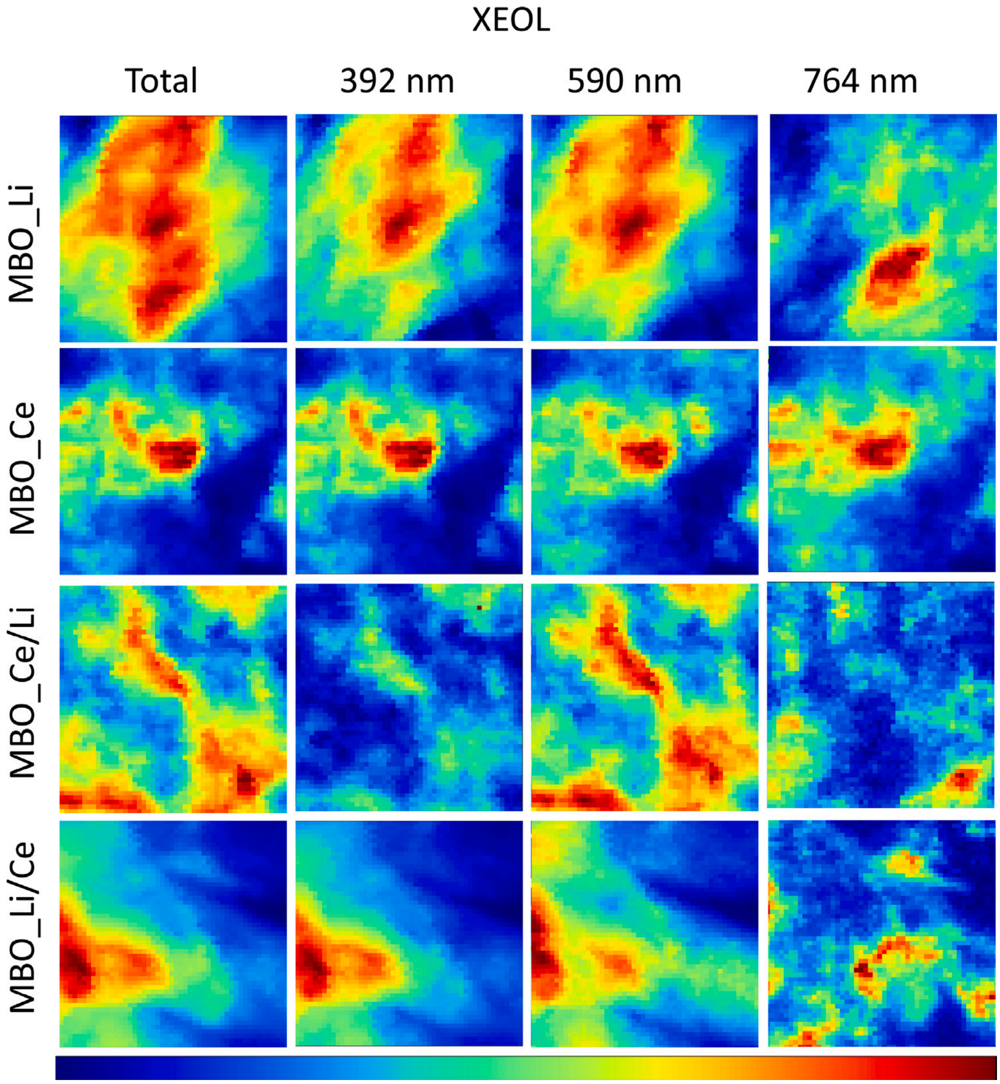

Fig. A.12. Comprehensive XEOL mapping of MgB_4O_7 with various dopant configurations (Ce-doped, Li-doped, and Ce/Li co-doped) alongside specific emission profiles at 392, 590, and 764 nm. The maps reveal distinct emission characteristics for each dopant combination. This spectral distribution demonstrates the synergistic effect of Li/Ce co-doping on optimizing luminescence in the MgB_4O_7 host matrix. MBO-Ce/Li = MgB_4O_7:$Ce_{0.67}Li_{0.33}$ and MBO-Li/Ce = MgB_4O_7:$Ce_{0.33}Li_{0.67}$.

References

[1] J. Liu, Z. Yang, B. Ye, Z. Zhao, Y. Ruan, T. Guo, X. Yu, G. Chen, S. Xu, A review of stability-enhanced luminescent materials: fabrication and optoelectronic applications, J. Mater. Chem. C 7 (17) (2019) 4934–4955.

[2] O. Ostroverkhova, Organic optoelectronic materials: mechanisms and applications, Chem. Rev. 116 (22) (2016) 13279–13412.

[3] E.G. Yukihara, S.W. McKeever, C.E. Andersen, A.J. Bos, I.K. Bailiff, E.M. Yoshimura, G.O. Sawakuchi, L. Bossin, J.B. Christensen, Luminescence dosimetry, Nat. Rev. Methods Prim. 2 (1) (2022) 26.

[4] R. Contassot, J. Batista, A. Otsuka, A. Souza, E. Ferraz, A.S. Souza, J.L. Santos, V. Coelho, H. Lima, Elucidating the effect of intrinsic defects on the dosimetric properties of the MgB4O7 compound: an atomistic simulation approach, New J. Chem. 46 (14) (2022) 6403–6413.

[5] E. Yukihara, B. Doull, T. Gustafson, L. Oliveira, K. Kurt, E. Milliken, Optically stimulated luminescence of MgB4O7:Ce,Li for gamma and neutron dosimetry, J. Lumin. 183 (2017) 525–532.

[6] E. Yukihara, E. Milliken, B. Doull, Thermally stimulated and recombination processes in MgB4O7 investigated by systematic lanthanide doping, J. Lumin. 154 (2014) 251–259.

[7] S. İflazoğlu, A. Yılmaz, V.E. Kafadar, M. Topaksu, A. Yazıcı, Neutron+ Gamma response of undoped and Dy doped MgB4O7 thermoluminescence dosimeter, Appl. Radiat. Isot. 147 (2019) 91–98.

[8] S. İflazoğlu, V.E. Kafadar, A. Yilmaz, Synthesis and thermoluminescence characterization of β-irradiated MgB4O7 phosphor co-doped with Dy and Na, J. Phys. Chem. Solids 197 (2025) 112450.

[9] L. Bossin, I. Plokhikh, J.B. Christensen, D.J. Gawryluk, Y. Kitagawa, P. Leblans, S. Tanabe, D. Vandenbroucke, E.G. Yukihara, Addressing current challenges in OSL dosimetry using MgB4O7: Ce, Li: state of the art, limitations and avenues of research, Materials 16 (8) (2023) 3051.

[10] T.D. Gustafson, E. Milliken, L. Jacobsohn, E. Yukihara, Progress and challenges towards the development of a new optically stimulated luminescence (OSL) material based on MgB4O7:Ce,Li, J. Lumin. 212 (2019) 242–249.

[11] L.F. Souza, A.L. Novais, P.L. Antonio, L.V. Caldas, D.N. Souza, Luminescent properties of MgB4O7:Ce,Li to be applied in radiation dosimetry, Radiat. Phys. Chem. 164 (2019) 108353.

[12] J.V. Batista, H. Trombini, A. Otsuka, I.S. Silveira, L.V. Caldas, A.O. de Souza, A.S. Souza, J.L. Santos, V. Coelho, H. Lima, Unlocking the effect of Li and Ce ions on the thermoluminescence and optically stimulated luminescence signals of the MgB4O7 compound, Dalton Trans. 52 (19) (2023) 6407–6419.

[13] N. Shrestha, D. Vandenbroucke, P. Leblans, E. Yukihara, Feasibility studies on the use of MgB4O7:Ce,Li-based films in 2D optically stimulated luminescence dosimetry, Phys. Open 5 (2020) 100037.

[14] I. Plokhikh, I.I. Sadykov, O.V. Safonova, Ł. Kondracki, E.G. Yukihara, L. Bossin, D.J. Gawryluk, Role of dopant concentration and starting reagents in the dosimetric performance of MgB4O7: Ce, Li, J. Lumin. 279 (2025) 121019.

[15] X. Cao, J. Qin, G. Gou, J. Li, W. Wu, S. Luo, Y. Luo, Z. Dong, J. Ma, Y. Long, Continuous solvent-free synthesis of imines over uip-γ-Al2O3-CeO2 catalyst in a fixed bed reactor, Appl. Catal. B: Environ. 272 (2020) 118958.

[16] S.J. Park, M.H. Joo, J.Y. Maeng, C.K. Rhee, J.-G. Kang, Y. Sohn, Electrochemical Ce3+/Ce4+ and Eu2+/Eu3+ interconversion, complexation, and electrochemical CO2 reduction on thio-terpyridyl-derivatized Au electrodes, Appl. Surf. Sci. 576 (2022) 151793.

[17] Z. Xie, F. Xiong, D. Zhou, Study of the Ce3+/Ce4+ redox couple in mixed-acid media (CH3SO3H and H2so4) for redox flow battery application, Energy Fuels 25 (5) (2011) 2399–2404.

[18] Y. Long, H. Zhang, Z. Gao, J. Qin, Y. Pan, J. Zhao, Y. Luo, Z. Ma, Y. Xiong, J. Ma, A protective roasting strategy for preparation of stable mesoporous hollow CeO 2 microspheres with enhanced catalytic activity for one-pot synthesis of imines from benzyl alcohols and anilines, Inorg. Chem. Front. 6 (3) (2019) 829–836.

[19] J. Zhang, J. Yang, J. Wang, H. Ding, Q. Liu, U. Schubert, Y. Rui, J. Xu, Surface oxygen vacancies dominated CeO2 as efficient catalyst for imine synthesis: Influences of different cerium precursors, Mol. Catal. 443 (2017) 131–138.

[20] S. Zhang, Z.-Q. Huang, Y. Ma, W. Gao, J. Li, F. Cao, L. Li, C.-R. Chang, Y. Qu, Solid frustrated-lewis-pair catalysts constructed by regulations on surface defects of porous nanorods of CeO2, Nat. Commun. 8 (1) (2017) 15266.

[21] H.C. Tolentino, R.R. Geraldes, F.M. da Silva, M.G.D. Guaita, C.M. Camarda, R. Szostak, I.T. Neckel, V.C. Teixeira, D. Hesterberg, C.A. Pérez, et al., The CARNAUBA X-ray nanospectroscopy beamline at the Sirius-LNLS synchrotron light source: Developments, commissioning, and first science at the TARUMA station, J. Electron Spectrosc. Relat. Phenom. 266 (2023) 147340.

[22] V.A. Solé, E. Papillon, M. Cotte, P. Walter, J. Susini, A multiplatform code for the analysis of energy-dispersive X-ray fluorescence spectra, Spectrochim. Acta Part B: At. Spectrosc. 62 (1) (2007) 63–68.

[23] N. Fairley, V. Fernandez, M. Richard-Plouet, C. Guillot-Deudon, J. Walton, E. Smith, D. Flahaut, M. Greiner, M. Biesinger, S. Tougaard, et al., Systematic and collaborative approach to problem solving using X-ray photoelectron spectroscopy, Appl. Surf. Sci. Adv. 5 (2021) 100112.

[24] E. Bêche, P. Charvin, D. Perarnau, S. Abanades, G. Flamant, Ce 3d XPS investigation of cerium oxides and mixed cerium oxide ($Ce_xTi_yO_2$), Surf. Interface Anal. 40 (3–4) (2008) 264–267.

[25] R. Megginson, F. Grillo, S.M. Francis, V.Z.C. Paes, H. Trombini, P.L. Grande, A.K. Rossall, J.A. van den Berg, C.J. Baddeley, Thermal behaviour of Cu and Au nanoparticles grown on CeO_2 thin films, Appl. Surf. Sci. 575 (2022) 151656.

[26] M.A. Goldberg, M.R. Gafurov, O.N. Makshakova, S.V. Smirnov, A.S. Fomin, F.F. Murzakhanov, V.S. Komlev, Peculiarities of charge compensation in lithium-doped hydroxyapatite, Heliyon 10 (4) (2024) e25291.

[27] L. Yin, S. Zhang, Y. Huang, C. Yan, Y. Du, Cerium contained advanced materials: Shining star under electrocatalysis, Coord. Chem. Rev. 518 (2024) 216111.

[28] C.E. Castano, M.J. O'Keefe, W.G. Fahrenholtz, Cerium-based oxide coatings, Curr. Opin. Solid State Mater. Sci. 19 (2) (2015) 69–76.

[29] T. Montini, M. Melchionna, M. Monai, P. Fornasiero, Fundamentals and catalytic applications of CeO2-based materials, Chem. Rev. 116 (10) (2016) 5987–6041.

[30] G.F. Bispo, D.S. Nascimento, L.B. Santana, G.S. Ferreira, Z.S. Macedo, H.R. Lima, S.O. Souza, F. d'Errico, R.A. Jackson, M.E. Valerio, Defects in MgB4O7 (pure and doped with lanthanides): A case study using a computational modelling approach, Phys. B 640 (2022) 414049.

[31] O. Annalakshmi, M. Jose, U. Madhusoodanan, J. Sridevi, B. Venkatraman, G. Amarendra, A. Mandal, Thermoluminescence mechanism in rare-earth-doped magnesium tetra borate phosphors, Radiat. Eff. Defects Solids 169 (7) (2014) 636–645.

[32] A.C. Silva, L.M. Amorim, A. Cruz, V.K. Asfora, V.S. de Barros, C.N. Oliveira, P.L. Guzzo, H.J. Khoury, Evaluation of TL and OSL signals of MgB4O7:Tm,Li prepared by the solution combustion method, Radiat. Meas. 173 (2024) 107099.

[33] Y. Uenaka, T. Uchino, Photoexcitation, trapping, and recombination processes of the F-type centers in lasing MgO microcrystals, Phys. Rev. B—Condens. Matter Mater. Phys. 83 (19) (2011) 195108.

[34] M. Kalinkin, D. Akulov, R. Abashev, A. Surdo, M. Kuznetsov, D. Kellerman, The role of defects in thermoluminescence of pure and rare-earth-doped magnesium tetraborate phosphor, J. Lumin. 263 (2023) 120119.

[35] S. Aškrabić, Z. Dohčević-Mitrović, V. Araújo, G. Ionita, M. De Lima, A. Cantarero, F-centre luminescence in nanocrystalline CeO2, J. Phys. D: Appl. Phys. 46 (49) (2013) 495306.

[36] D. Muñoz Ramo, J. Gavartin, A. Shluger, G. Bersuker, Spectroscopic properties of oxygen vacancies in monoclinic HfO2 calculated with periodic and embedded cluster density functional theory, Phys. Rev. B—Condens. Matter Mater. Phys. 75 (20) (2007) 205336.

[37] T. Konig, G.H. Simon, H.-P. Rust, G. Pacchioni, M. Heyde, H.-J. Freund, Measuring the charge state of point defects on MgO/Ag (001), J. Am. Chem. Soc. 131 (48) (2009) 17544–17545.

[38] J. Chen, L.-B. Lin, F.-Q. Jing, Theoretical study of F-type color center in rutile TiO2, J. Phys. Chem. Solids 62 (7) (2001) 1257–1262.

[39] A. Popov, E. Kotomin, J. Maier, Basic properties of the F-type centers in halides, oxides and perovskites, Nucl. Instrum. Methods Phys. Res. Sect. B: Beam Interact. Mater. Atoms 268 (19) (2010) 3084–3089.

[40] Z. Yang, S. Lai, Z. Xia, Self-activated luminescence in AZn4 (BO3) 3 (A=K, Rb, Cs) and oxygen-defects-related photoluminescence tuning, J. Solid State Chem. 288 (2020) 121408.

[41] H. Yu, D. Deng, W. Su, C. Li, S. Xu, Broadband near-infrared downconversion luminescence in Yb3+-doped BaZn2(BO3)2, Opt. Mater. 80 (2018) 160–168.

[42] V. Altunal, W. Abusaid, V. Guckan, A. Ozdemir, Z. Yegingil, Luminescence characterization of Ce and Gd doped MgB4O7 phosphors, J. Lumin. 246 (2022) 118815.

[43] N. Porwal, R. Kadam, T. Seshagiri, V. Natarajan, A. Dhobale, A. Page, EPR and TSL studies on MgB4O7 doped with Tm: role of BO32- in TSL glow peak at 470 K, Radiat. Meas. 40 (1) (2005) 69–75.

[44] T. Aitasalo, J. Hölsä, M. Lastusaari, J. Niittykoski, F. Pellé, Delayed luminescence of Ce3+ doped X1 form of Y2SiO5, Opt. Mater. 27 (9) (2005) 1511–1515.

[45] T. Aitasalo, J. Hölsä, M. Lastusaari, J. Legendziewicz, J. Niittykoski, F. Pellé, Delayed luminescence of Ce3+ doped Y2SiO5, Opt. Mater. 26 (2) (2004) 107–112.

[46] T. Aitasalo, J. Hölsä, M. Lastusaari, J. Niittykoski, F. Pellé, Defects in Ce3+ doped Y2SiO5, Phys. Status Solidi (C) 2 (1) (2005) 272–275.

[47] A. Oza, V. Ojha, S. Dhale, S. Dhoble, Photoluminescence and thermoluminescence in Dy3+-, Ce3+-, and Tb3+-activated MgB4O7 phosphor for dosimetry application, Luminescence 37 (9) (2022) 1563–1574.

[48] D. de Vasconcelos, M. Souza, I. Silveira, E. Zanotto, L. Caldas, Ce-doped magnesium borate glass-ceramic for optically stimulated luminescence dosimetry, Ceram. Int. 50 (23) (2024) 48988–48994.

[49] I.S. Gaona, S.S. Vera, H. Khoury, V. Asfora, V. De Barros, J. Roa-Rojas, C.P. Vargas, W. Jaramillo-Garzón, Effect of route production and doping concentration on luminescence response of MgB4O7: Gd phosphor, J. Lumin. 266 (2024) 120320.

[50] G. Blasse, B. Grabmaier, G. Blasse, B. Grabmaier, A General Introduction to Luminescent Materials, Springer, 1994.

[51] Z. Li, N. Xu, Y. Zhang, W. Liu, J. Wang, M. Ma, X. Fu, X. Hu, W. Xu, Z.-K. Han, Unveiling the structure of oxygen vacancies in bulk ceria and the physical mechanisms behind their formation, J. Phys. Chem. Lett. 15 (22) (2024) 5868–5874.

[52] G. Zhou, W. Geng, L. Sun, X. Wang, W. Xiao, J. Wang, L. Wang, Influence of mixed valence on the formation of oxygen vacancy in cerium oxides, Materials 12 (24) (2019) 4041.

[53] M.V. Ganduglia-Pirovano, A. Hofmann, J. Sauer, Oxygen vacancies in transition metal and rare earth oxides: Current state of understanding and remaining challenges, Surf. Sci. Rep. 62 (6) (2007) 219–270.

[54] C. Zhang, A. Michaelides, D.A. King, S.J. Jenkins, Oxygen vacancy clusters on ceria: Decisive role of cerium f electrons, Phys. Rev. B—Condens. Matter Mater. Phys. 79 (7) (2009) 075433.

[55] T. Li, S. Quan, X. Shi, C. Liu, L. Yang, Photocatalytic activity of bi2o3 enhanced by the addition of Ce3+/Ce4+ synthesized by ethylene glycol-assisted solvothermal method, ChemistrySelect 5 (19) (2020) 5799–5808.

[56] Y.-H. Cui, Y.-J. Feng, Z.-Q. Liu, Influence of rare earths doping on the structure and electro-catalytic performance of Ti/Sb–SnO2 electrodes, Electrochim. Acta 54 (21) (2009) 4903–4909.

[57] Q. Zhou, L. Dolgov, A.M. Srivastava, L. Zhou, Z. Wang, J. Shi, M.D. Dramićanin, M.G. Brik, M. Wu, Mn2+ and Mn4+ red phosphors: synthesis, luminescence and applications in WLEDs. A review, J. Mater. Chem. C 6 (11) (2018) 2652–2671.

[58] T. Zhijian, L. Tingting, G. Li, C. Zhang, L. Xiaowei, L. Daling, T. Qiang, Comparison of thermoluminescence spectra of MgB4O7 doped with dysprosium and manganese, J. Rare Earths 31 (11) (2013) 1039–1042.

[59] A. Ozdemir, V. Altunal, V. Guckan, K. Kurt, Z. Yegingil, Luminescence characteristics of newly-developed MgB4O7: Ce3+,Na+ phosphor as an OSL dosimeter, J. Alloys Compd. 865 (2021) 158498.

[60] B. Su, G. Zhou, J. Huang, E. Song, A. Nag, Z. Xia, Mn2+-doped metal halide perovskites: structure, photoluminescence, and application, Laser Photonics Rev. 15 (1) (2021) 2000334.

[61] R.K. Chandrakar, R. Baghel, V. Chandra, B. Chandra, Synthesis, characterization and photoluminescence studies of Mn doped ZnS nanoparticles, Superlattices Microstruct. 86 (2015) 256–269.

[62] S. Das Adhikari, A.K. Guria, N. Pradhan, Insights of doping and the photoluminescence properties of Mn-doped perovskite nanocrystals, J. Phys. Chem. Lett. 10 (9) (2019) 2250–2257.

[63] A. Ozdemir, Z. Yegingil, N. Nur, K. Kurt, T. Tuken, T. Depci, G. Tansug, V. Altunal, V. Guckan, G. Sigircik, et al., Thermoluminescence study of mn doped lithium tetraborate powder and pellet samples synthesized by solution combustion synthesis, J. Lumin. 173 (2016) 149–158.

[64] O. Annalakshmi, M. Jose, G. Amarendra, Dosimetric characteristics of manganese doped lithium tetraborate–An improved TL phosphor, Radiat. Meas. 46 (8) (2011) 669–675.

[65] I. Plokhikh, Ł. Kondracki, E.G. Yukihara, D.J. Gawryluk, L. Bossin, Impact of sample preparation temperature on Li and Ce co-doped MgB4O7 dosimetry performance: A plausible scenario for controlling defect clustering, J. Lumin. 275 (2024) 120784.

[66] T. Jintakosol, P. Singjai, Effect of annealing treatment on luminescence property of MgO nanowires, Curr. Appl. Phys. 9 (6) (2009) 1288–1292.